APPLIED SCIENCES AND ENGINEERING

Nanobubble-controlled nanofluidic transport

Jake Rabinowitz[1], Elizabeth Whittier[1], Zheng Liu[2], Krishna Jayant[1,2]*,
Joachim Frank[2], Kenneth Shepard[1,3]†

Nanofluidic platforms offering tunable material transport are applicable in biosensing, chemical detection, and filtration. Prior studies have achieved selective and controllable ion transport through electrical, optical, or chemical gating of complex nanostructures. Here, we mechanically control nanofluidic transport using nanobubbles. When plugging nanochannels, nanobubbles rectify and occasionally enhance ionic currents in a geometry-dependent manner. These conductance effects arise from nanobubbles inducing surface-governed ion transport through interfacial electrolyte films residing between nanobubble surfaces and nanopipette walls. The nanobubbles investigated here are mechanically generated, made metastable by surface pinning, and verified with cryogenic transmission electron microscopy. Our findings are relevant to nanofluidic device engineering, three-phase interface properties, and nanopipette-based applications.

INTRODUCTION

Surface-pinned nanobubbles (*1*), nanoscale air pockets residing at liquid-solid interfaces, defy physical (*2*, *3*) and thermodynamic (*4*) predictions of instantaneous dissolution. Experimental recordings attribute long nanobubble lifetimes to liquid oversaturation with gas (*5*, *6*), small three-phase contact angles (*1*), contact line pinning (*7*), and gas accumulation at three-phase interfaces (*8*, *9*). Across these mechanisms, a common feature is the reduction of the gas-phase concentration gradient between the nanobubble surface and the bulk gas-saturated solution.

In nanofluidic channels, surface-pinned nanobubbles present many applications. These nanobubbles can impede (*10*), gate (*11*, *12*), rectify (*13*, *14*), or enhance (*15*) ion transport; elsewhere, they can drive selective mass transport (*16*, *17*). These prior efforts manipulate nanobubbles using chemical, electrical, optical, and/or evaporative techniques. Inspired by biological ion channels (*18*), much related work has enhanced nanofluidic transport capabilities by modifying nanochannel walls to manipulate surface wettability or ionic double layer properties (*19*–*24*). In broader application domains, nanobubbles are relevant to water treatment (*16*, *25*), mineral recovery (*26*), energy harvesting (*27*), electrochemistry (*28*), targeted imaging and drug delivery (*29*), and plant biology (*30*).

Here, we study how nanobubbles control nanofluidic transport. In our experiments, metastable nanobubbles plug nanopipette channels and divert electrolyte flows through interfacial electrolyte films. Negatively charged nanobubble surfaces induce ion concentration enrichment and depletion in these films to rectify ionic currents (*31*, *32*). Enrichment and depletion occur at concentrations up to 3 M KCl, where (rectifying) nanobubble-plugged pipettes are clearly distinguished from (linear) nanobubble-free pipettes. Supporting this depiction, nanobubble presence inside nanopipettes is confirmed by cryo–electron microscopy (cryo-EM) using the transmission electron microscope. In the forward rectifying direction, nanobubbles enhance ionic currents (*15*) when sufficiently strong concentration enrichment drives nonlinear electroosmotic flows (*33*–*35*). Long-term monitoring of nanobubble-plugged nanopipettes confirms nanobubble metastability and slow growth, which are further supported by a numerical model.

RESULTS

Nanobubble detection and cryo-EM verification

We first measured ionic currents through a set (*n* = 42) of uniformly prepared nanopipettes filled with neutral-buffered 3 M KCl (fig. S1). In such highly concentrated electrolyte, electroosmotic flow and the ionic double layer minimally influence ion transport (*31*, *35*). Thus, electrophoresis and bulk electrolyte properties determine the nanochannel's current-voltage response.

Under these conditions, properly wetted nanochannels as small as a few nanometers in aperture present linear current-voltage responses (*35*, *36*). However, 57% of our measurements yielded rectified current-voltage responses (fig. S1). We attribute these data to the presence of nanobubbles inside the nanopipettes, which results in incomplete nanochannel wetting and surface-governed ion transport.

The rectifying nanopipettes all share the same direction of ion current rectification and are generally more resistive than the linear nanopipettes (fig. S1, inset). The rectification behavior is consistent with negatively charged nanobubble surfaces (*26*, *37*) restricting anion flow and inducing voltage-dependent ion concentration enrichment or depletion (*15*, *32*, *35*, *38*, *39*). The increased resistances are consistent with nanobubbles excluding electrolyte and reducing the effective size of the nanopipette tip (*10*–*14*). These results persist across many different nanopipette and nanobubble sizes (fig. S1).

Nanobubble metastability is confirmed by the reproducibility of rectified ionic current measurements over consecutive voltage sweeps. Because changing nanobubble configurations are evident in altered ionic current measurements (*15*), overlapping recordings in our work show these nanobubbles to be stable for at least the minute-long measurement time scale.

We further confirmed nanobubble occupancy inside nanopipettes using cryo-EM. Between ionic current recording and EM imaging, nanopipette tips were grid-mounted and cryogenically frozen to preserve the as-measured nanofluidic systems (fig. S2) (*40*–*42*). Because the EM signal is dependent on mass density, nanobubbles in micrographs appear lighter than liquid and solid materials.

[1]Department of Electrical Engineering, Columbia University, New York, NY 10027, USA. [2]Department of Biological Sciences, Columbia University, New York, NY 10027, USA. [3]Department of Biomedical Engineering, Columbia University, New York, NY 10027, USA.
*Present address: Department of Biomedical Engineering, Purdue University, West Lafayette, IN 47907, USA.
†Corresponding author. Email: shepard@ee.columbia.edu

A micrograph of a representative nanobubble-plugged nano-pipette and its rectified ionic current measurement are shown (Fig. 1A). The conical nanopipette extends downward from the top of the micrograph. Gaseous nanobubbles (lightest regions), solid glass walls (darkest regions), and liquid electrolyte are depicted. The lower nanobubbles (directly inside the pipette tip) have diameters of ~9 nm; the top nanobubble (pinned to the left side of the inner channel) is 7 nm in diameter. Ionic currents displayed in Fig. 1A (and throughout) are averaged from consecutive recordings, with error bars showing SDs.

Micrographs of control nanopipettes are provided (Fig. 1, B and C). A representative nanobubble-free nanopipette and its corresponding linear ionic current measurement are shown (Fig. 1B). An air-filled nanopipette is shown as an additional control (Fig. 1C). Other nanobubble micrographs are provided to illustrate the reproducibility of the imaging procedure (Fig. 1D).

Electronic characterization of nanobubble-plugged nanochannels

We are precluded from definitively correlating EM-recorded nano-bubble geometries with ionic current measurements because of the possibility that nanobubble configurations change between ionic current measurements and imaging. Instead, we analyzed several electronic measurements made for different nanobubble configurations to determine how nanobubble sizes influence nanofluidic transport.

In these measurements, we used a simple procedure to modify nanobubble configurations within a single nanopipette. This procedure allows for direct comparison of ionic transport in nanobubble-plugged and nanobubble-free conditions and across varying nano-bubble configurations. The method relies on the stochastic competition between surface tension and hydrostatic forces to yield partially wetted (e.g., nanobubble-plugged) nanopipettes.

We begin experiments by filling nanopipettes with electrolyte while holding the tips exposed to air. Under these conditions, surface tension keeps the nanoscopic and hydrophobic tips filled with air, as evidenced by the immeasurably small conductivity when such nano-pipettes are immersed in equivalent electrolyte baths (fig. S3). With removal and reimmersion of these pipettes into the electrolyte, hydrostatic pressure drives additional electrolyte into the tip, while surface tension competes to maintain air voids. The mechanical competition is stochastic, typically creating nanobubbles with vary-ing sizes and occasionally wetting the nanochannel completely.

We demonstrate nanobubble generation and influence on nano-fluidic transport with a representative series of nanobubble-plugged (trials 1 to 3) and nanobubble-free (trial 4) ionic current measure-ments for a single nanopipette in 3 M KCl (Fig. 2A). We observed size-dependent changes to the nanopipette's fluidic response when-ever nanobubbles were present, demonstrating that any nanobubble plug modifies the transport behavior as compared to a properly wetted nanochannel. The rectifying and linear current measurements were repeatable while maintaining pipette-electrolyte immersion and modifiable with pipette removal and reimmersion. The wide variation in rectifying transport characteristics (trials 1 to 3) shows the strong dependence of nanofluidic transport on the nanobubble size. The constant resistance in trial 4 is consistent with the expected value for a nanobubble-free nanochannel given the electrolyte resis-tivity and the nanopipette geometry (fig. S4).

Varied ionic currents across different nanobubble configurations (Fig. 2A) allow us to infer relative nanobubble heights (Fig. 2A, inset). If we assume that nanobubble radii are equal to that of the inner nanochannel, the long and narrow tip geometry results in the ionic current primarily depending on the nanobubble's height. Larger nanobubbles exclude more electrolyte and provide more area for surface-governed transport, respectively, increasing the nanopipette's resistance and ion rectification ratio. We quantify ion current recti-fication by defining a rectification ratio (RR) as the larger over the smaller current magnitudes at ±0.9 V. Progressing from trials 1 to 4, nanopipette resistances and rectification ratios show correlated
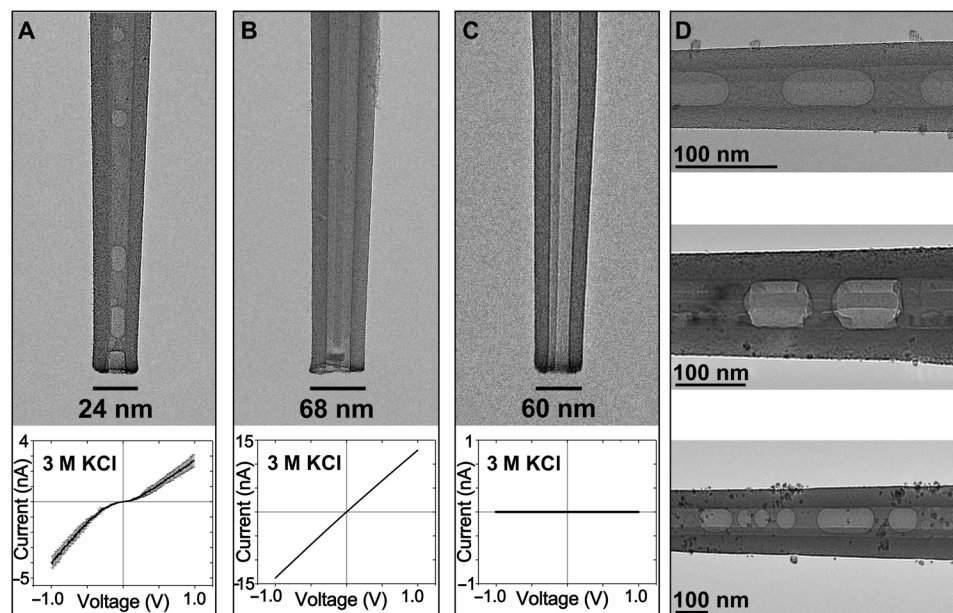
Fig. 1. Nanobubble-induced ion current rectification. (**A** to **C**) Cryogenic transmission electron micrographs and corresponding ionic current measurements for (A) a nanobubble-plugged nanopipette, (B) a nanobubble-free nanopipette, and (C) an air-filled nanopipette. (**D**) Additional nanobubble micrographs.
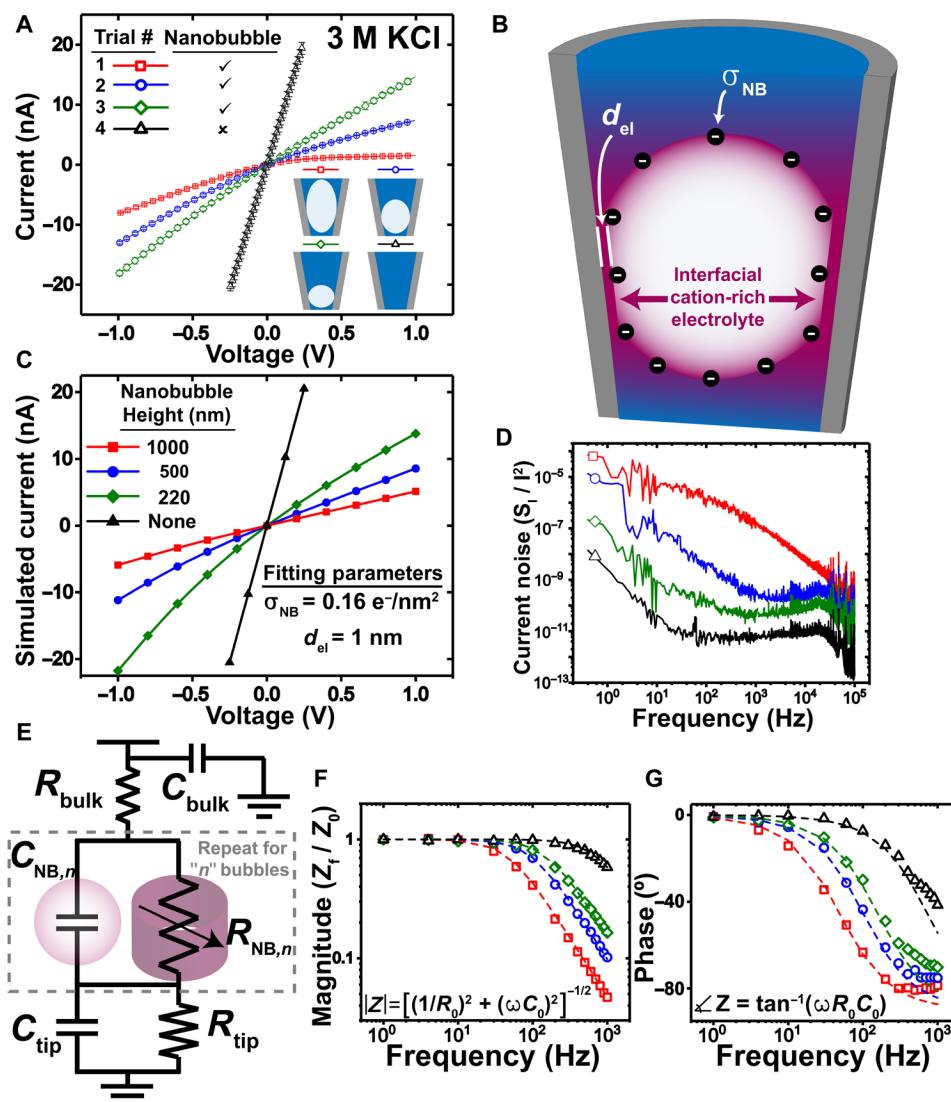
Fig. 2. Electronic characterization of a nanobubble-plugged nanochannel. (**A**) Ionic currents through a single nanopipette in 3 M KCl, with relative nanobubble sizes. (**B**) Nanobubbles induce surface-governed ion transport through interfacial electrolyte films (thickness, d_{el}) enriched with cations by the nanobubble surface charge (σ_{NB}). (**C**) Finite element simulation of ion transport in (A). (**D**) Normalized current noise spectra for nanobubble configurations in (A). (**E**) Equivalent circuit representation of nanofluidic model in (B). The interfacial electrolyte resembles a voltage-dependent resistor. The nanobubble resembles a shunt capacitor. (**F** and **G**) AC impedance measurements (symbols) for nanopipette configurations in (A), fit to single-element parallel R-C circuit transfer functions (lines).

reductions (table S1), as improved nanochannel wetting decreases electrolyte exclusion and ion concentration enrichment/depletion. Therefore, nanobubble heights decrease across trials 1 to 3 before complete nanopipette wetting is observed in trial 4.

A model for the nanobubble-plugged nanopipette depicts electrolyte transport through a thin interfacial film (thickness, d_{el}) between the nanobubble and the nanochannel wall (Fig. 2B). The nanobubble's negative surface charge (σ_{NB}) enriches the interfacial electrolyte with cations (red color) and rectifies currents by restricting anion transport. This anionic transport restriction results in voltage-dependent concentration enrichment (depletion) when anions are driven to exit (enter) the nanopipette (*31*). Because the enrichment and depletion effects occur in high ionic strength conditions, it is likely that the interfacial electrolyte thickness is comparable to the experimental Debye length (<0.5 nm in 3 M KCl). Induced charge

redistribution along the nanobubble surface (*32*, *33*, *35*) further exacerbates this voltage-dependent ion enrichment and depletion. The enrichment and depletion effects are rapid, as the nanopipette's current response is independent of the voltage sweep rate up to 1 V/ms (fig. S5).

Ion transport simulations (Fig. 2C) support our nanobubble height depictions (Fig. 2A) and nanofluidic model (Fig. 2B). We simulate ionic currents by solving the coupled Poisson-Nernst-Planck equations through a conical nanochannel with dimensions as in fig. S4. After fitting the model to match the linear transport in Fig. 2A, we replicate experimental trends by simulating current-voltage responses with increasingly large nanobubbles in the center of the nanopipette (Fig. 2C; simulation details in fig. S6 and table S2). These simulations support the electrolyte exclusion model by predicting that larger nanobubbles induce greater current reductions. They likewise

support the concentration enrichment and depletion model by predicting that more highly charged nanobubbles and thinner interfacial electrolytes yield larger ion rectification ratios (fig. S7).

The simulation accuracy indicates that electroosmosis minimally influences the ionic current measurements in Fig. 2A. Consistent with prior modeling of concentrated and uniform electrolytes (31, 35), this result leaves ion transport to be governed by electrophoresis, electrolyte exclusion, and concentration enrichment/depletion. Although results below suggest that electroosmosis cannot always be neglected, the continuum approach cannot model these electroosmotic flows because the interfacial electrolyte is not sufficiently thicker than the mean free path of a water molecule (0.28 nm).

Current noise measurements (Fig. 2D) for the nanobubble configurations of Fig. 2A further support our geometric nanobubble descriptions. Nanobubble presence increases the nanopipette's flicker noise power and cut-off frequency (Fig. 2D and table S1) (10). Prior analysis of nanopore flicker noise attributes this phenomenon to ion adsorption/desorption in response to surface charge fluctuations (43). We infer physical nanobubble properties from the noise measurements using Hooge's relation, $\frac{S_I}{I^2} = \frac{\alpha}{f^\beta}$, where S_I is the current noise power, I is the average current magnitude, f is the frequency, α is inversely proportional to ion count, and β is inversely proportional to surface trapping frequency (36).

Hooge parameters relate the current noise measurements to our proposed nanobubble heights. Larger nanobubbles more drastically lower the available ion count, inducing greater increases in noise power (higher α). Larger nanobubbles also introduce more surface area for ion adsorption/desorption, inducing slower frequency-dependent reductions in noise power (lower β) (Fig. 2D and table S1).

Other characteristics of these noise spectra are consistent with a nanobubble-plugged channel. The nanobubble-induced noise spectra show voltage dependencies (fig. S8) due to the voltage-dependent surface charge distributions (33, 35). In other words, surface charge polarization alters the available ion count (α) in the interfacial electrolyte and the ion adsorption/desorption properties (β). At large voltages (±1 V), nanobubbles induce low-frequency current drift and random telegraph noise (fig. S9). These conductance fluctuations may arise from a nanopore effect in which dielectric image charges alter ion solvation properties (44). In support of this idea, we note that a thin electrolyte residing between solid and vapor dielectrics would yield a relatively large ratio of image charge density to ion density.

An equivalent circuit model for the model nanofluidic pathway (Fig. 2B) depicts the nanobubble-plugged region as a parallel R-C network (Fig. 2E). Within this physical circuit, the nanobubble is modeled as a capacitor (C_{NB}) and the interfacial electrolyte (approximated as a cylindrical shell) is modeled as a voltage-dependent resistor (R_{NB}). This R-C network repeats in series for the possible case of multiple nanobubbles. Above and below the nanobubble(s), bulk electrolytes in the nanopipette interior and tip present additional resistances. In parallel to these resistances, the pipette sidewalls present distributed capacitances to the grounded bath electrolyte.

AC impedance measurements (Fig. 2, F and G, symbols) agree with impedance simulations (Fig. 2, F and G, lines) incorporating the relative nanobubble heights in Fig. 2A. During impedance simulations, we use directly measured resistances (R_0) and single-pole R-C transfer functions (listed) to fit capacitances (C_0) to the experimental systems (table S1). Capacitances reduce across trials 1 to 4, revealing nanobubbles to be shunt capacitors (fig. S10) consistent

with their small size. Because a nanobubble is connected in series and presents a considerably smaller capacitance than a nanopipette tip (C_{tip}), impedance magnitudes are reduced and phase shifts are increased for nanobubble-plugged nanopipettes (Fig. 2, F and G, and table S1). Larger nanobubbles necessarily reside further inside the nanopipette, such that tip capacitance shunting is proportional to the nanobubble heights depicted in Fig. 2A. Accurate representations of the experimental systems with single-unit R-C equivalent circuits suggest that even in the possible presence of many nanobubbles, the largest nanobubble dominates the net response of the nanochannel.

We completed our characterization of nanobubble-plugged nanochannels by investigating the pH-dependence of ion current rectification in these systems. Prior works have shown the ability to tune the rectifying behavior of nanochannels by inducing surface modifications through pH-dependent chemistry (20, 23). Here, we assess nanobubble surface charge in acidic and basic 3 M KCl, noting that the nanobubble charge arises from surface hydroxide adsorption (37) and has been shown to become positive at low pH (26). Under drastically reduced hydroxide conditions (pH 2), our confined nanobubbles remained negatively charged (fig. S11), indicating a very high affinity for hydroxide adsorption. Under drastically increased hydroxide conditions (pH 12), nanobubble charge density was increased to yield an improved rectification ratio of 8.2 in 3 M KCl (fig. S11).

Nanobubble-enhanced ion conductance

These confined nanobubbles can increase ionic currents in the forward rectifying direction (15). Across a range of electrolyte concentrations (3 M to 5 mM), nanobubble-plugged nanopipettes exhibited increased forward-direction conductivities as compared to values measured in the nanobubble-free states (Fig. 3). These nanobubble configurations continue to impede ion currents in the reverse directions to further enhance rectification ratios.

With the same measurement procedure as shown in Fig. 2A, we observed nanobubble-enhanced ion conductance in 3 M KCl (Fig. 3A). These recordings depict three disparate nanobubble configurations (trials 1, 2, and 4) along with two overlapping nanobubble-free configurations (trials 3 and 5). The rectification ratios are noted, with small-signal conductances provided (fig. S12). In trials 2 and 4, nanobubbles enhanced ion conductivities for negative voltages larger than −0.25 V and drove larger currents than the nanobubble-free conditions (Fig. 3A, inset). For these nanopipettes, we define a conductance enhancement factor as the ratio of the maximum nanobubble-plugged conductance to the maximum nanobubble-free conductance. Trials 2 and 4 achieved conductance enhancement factors of 1.20 and 1.15, respectively.

We attribute nanobubble-induced current enhancement to nonlinear electroosmotic flows driven by ion concentration enrichment. When sufficiently strong concentration enrichment occurs, the resulting concentration gradient will induce a spatially inhomogeneous Debye length (31) that causes electroosmotic flows to scale exponentially with applied voltage (35). In the case of conductance enhancement, such flows contribute supplemental ionic currents in excess of those lost because of electrolyte exclusion. These flows are also uninhibited along the nanobubble surface, where the gas-liquid interface obviates the no-slip boundary constraint (45). In the reverse direction of rectification, concentration depletion drives the same electrokinetic effects to further impede flows and increase the ion rectification ratio (35).
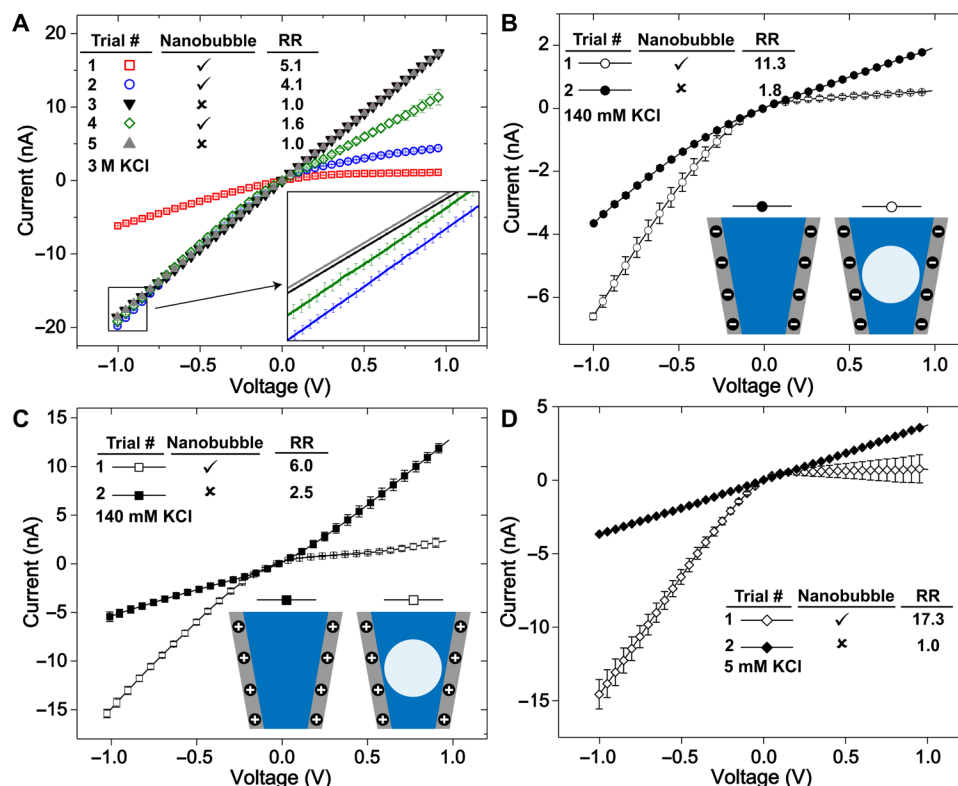
Fig. 3. Nanobubble-induced ion current enhancement. (**A**) Ionic currents through a single nanopipette in 3 M KCl. Inset: Nanobubbles enhance current magnitudes. (**B**) Ionic currents through a single nanopipette in 140 mM KCl. At the lower ionic strength, the nanobubble induces stronger current enhancement and rectification. (**C**) Ionic currents through a positively charged nanopipette in 140 mM KCl resemble a bipolar nanofluidic diode with polarity determined by the presence or absence of a nanobubble. (**D**) Ionic currents through a single nanopipette in 5 mM KCl demonstrate further increases in current enhancement and rectification with greater electrolyte dilution.

The conductance enhancement results in Fig. 3A support our physical description based on trial 2, showing stronger conductance enhancement and a greater rectification ratio than trial 4. Further comparison with trial 1 makes clear that only certain nanobubble configurations yield this effect. We speculate that these configurations include two closely spaced nanobubbles (e.g., Fig. 1D) or a nanobubble pinned to only one side of the nanopipette (e.g., Fig. 1A).

The physical model for conductance enhancement predicts the effect to be stronger in less concentrated electrolyte, where similarly charged surfaces induce relatively stronger concentration gradients. Because comparing absolute conductances across electrolyte concentrations is difficult, we verify this prediction by comparing rectification ratios and conductance enhancement factors across varying electrolyte concentrations.

Stronger conductance enhancement and ion current rectification were achieved for a nanobubble in 140 mM KCl (Fig. 3B; small-signal conductances in fig. S12). Under these conditions, a conductance enhancement factor of 1.7 and a rectification ratio of 11.3 were recorded. These results clearly indicate the presence of a nanobubble, which might have otherwise been obscured by the fact that small enough nanopipettes naturally rectify currents when completely wetted with 140 mM KCl (*31, 35*).

The intrinsic nanopipette rectification in 140 mM KCl allows us to substantiate nanobubbles as the source of the conductance enhancement. In a new experiment, we coated a nanopipette interior with poly-L-lysine (*46*) to positively charge the inner walls and invert the nanobubble-free rectification (Fig. 3, B and C, closed symbols).

Upon introducing a nanobubble, the nanopipette reverted back to favoring negative current (Fig. 3C, open symbols). The net response of the system resembles a bipolar diode that favors positive current without nanobubbles (driven by the positive wall charge) and negative current with nanobubbles (driven by the negative bubble charge). The nanobubble-plugged response again shows stronger rectification than the nanobubble-free response, as well as a conductance enhancement factor of 1.4 (small-signal conductances in fig. S13). Compared to Fig. 3B, we attribute the lower rectification ratio and conductance enhancement in Fig. 3C to the competing influences of the positively charged wall and the negatively charged nanobubble.

With further dilution, a nanobubble in 5 mM KCl yields even stronger conductance enhancement and rectification (Fig. 3D; small-signal conductances in fig. S14). Under these conditions, a conductance enhancement factor of 4.6 and a rectification ratio of 17.3 were recorded. We note that this experiment used a larger pipette to more clearly contrast the nanobubble-induced and nanobubble-free responses, as the intrinsic nanopipette rectification is strengthened in 5 mM electrolyte.

We directly compare the concentration dependence of nanobubble conductance enhancement using a dimensionless ratio of surface (κ^σ) to bulk (κ^L) conductance. At each concentration, we subtracted the nanobubble-free conductance from the nanobubble-enhanced conductance to calculate the minimum surface conductance contributed by the nanobubble (*47*). These values represent minima because they do not include nanobubble-induced losses in bulk conductance resulting from electrolyte exclusion. We then

calculated normalized conductance ratios by dividing the surface conductances by the same bulk conductances (κ^σ/κ^L). Surface-to-bulk conductance ratios of 0.2, 0.95, and 3.6 were observed for the unmodified nanopipettes in 3 M, 140 mM, and 5 mM conditions, respectively. Our minimum reported ratio in 5 mM conditions is comparable to that observed in surface charge–governed transport through a nanopore (48).

Nanobubble metastability model

Reproducible and geometry-dependent measurements in Figs. 1 to 3 demonstrate these nanobubbles to be stable for at least minutes and unperturbed by electric fields. Long-term monitoring of nanobubble-plugged nanopipettes reveals slow nanobubble growth.

We measured 5 days of nanobubble growth based on steadily reduced ionic currents (Fig. 4A; postmeasurement nanopipette micrograph in fig. S15). Initially, a nanopipette filled with 3 M KCl exhibited a rectification ratio of 1.3 and an average resistance of 54 megohms. Thereafter, ionic measurements were recorded, while the system was otherwise unperturbed. Over 5 days, the average resistance consistently increased to exceed 1 gigohm, while rectification ratios remained between 1.4 and 1.7 (fig. S16). We estimated the dynamically recorded nanobubble heights (Fig. 4A, inset) by

repeating the finite element procedure in Fig. 2C for the relevant nanopipette geometry and ionic current data (fig. S17).

Repeating the same experiment with a new nanopipette, a larger initial nanobubble (fig. S18; RR = 2.7, R_{avg} = 116 megohms) grew more quickly. Specifically, the resistance and rectification ratio largely increased within 30 min (fig. S18, inset). The nanobubble continued to grow over the next hour, with the resistance settling to a higher value (R_{avg} = 600 megohms) and the rectification ratio lowering to match the initial value (RR = 2.8).

Nanobubble growth is most readily achieved within gas over-saturated liquid (1, 6). Other reports of growing nanobubbles required drying and cavitation (49, 50). It is thus unexpected to observe nanobubble growth in our open system with free gas exchange and minimal volume losses in fluid reservoirs. We explain this growth with a dynamic equilibrium model for nanobubble-electrolyte gas exchange (8). In this model, gas efflux that occurs at the nanobubble's spherical caps is counterbalanced and exceeded by gas influx through its intermediate cylindrical region (Fig. 4B). Larger nanobubbles grow more quickly because higher aspect ratios provide greater ratios of influx to efflux.

Assuming that Henry's law and Laplace pressure remain valid for nanobubbles below 10 nm in radius (1, 28, 50), we describe the
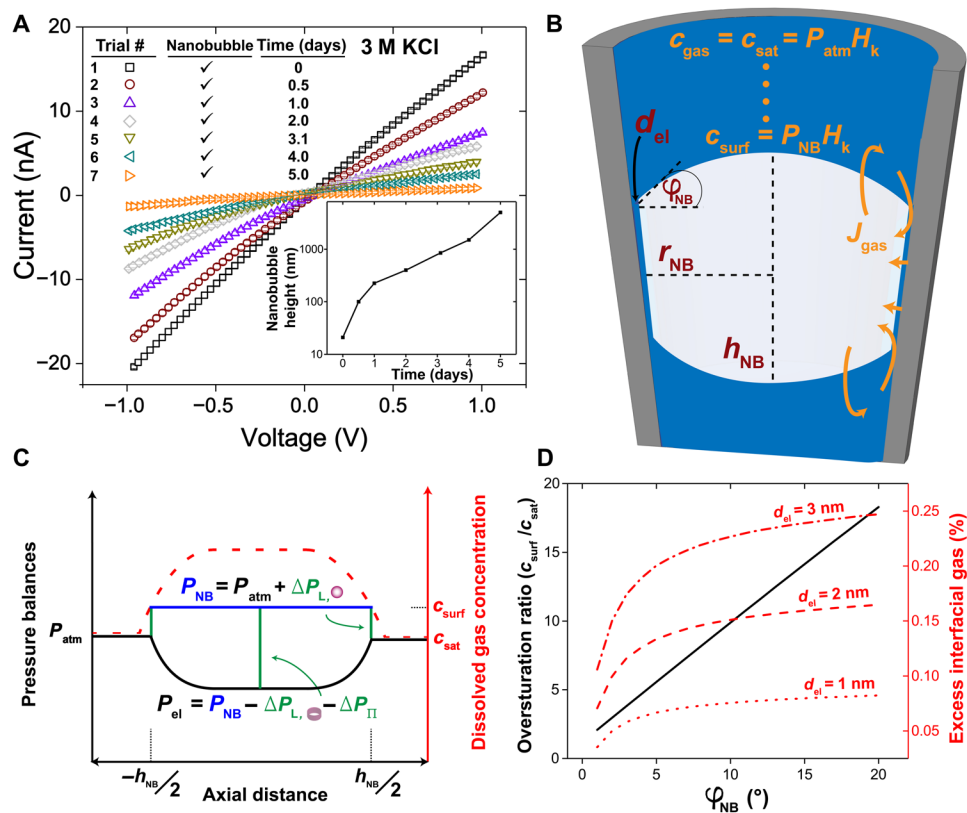

Fig. 4. Nanobubble metastability. (**A**) Ionic currents through an otherwise unperturbed nanobubble-plugged nanopipette. The nanobubble grows for 5 days before settling to a low-conducting state, with dynamic bubble heights estimated (inset). (**B**) Nanobubble-electrolyte gas exchange (J_{gas}). Efflux occurs through spherical caps and influx occurs through the interfacial electrolyte. Flux magnitudes depend on the interfacial gas concentration (c_{surf}) determined by the contact angle (φ_{NB}) and radius (r_{NB}). (**C**) Pressure balances (left axis) describe the electrolyte (black curve) and nanobubble (blue line) pressures according to two-phase pressure differences (green lines). Dissolved gas concentrations (right axis, red dashed curve) determine influx and efflux regimes in (B). (**D**) Gas oversaturation ratio at the nanobubble surface versus contact angle (left axis, solid line). The dissolved gas concentration in the interfacial electrolyte drives influx by slightly exceeding the surface concentration (right axis) and depends on the interfacial electrolyte thickness (dashed and dotted curves).

dissolved gas concentration at the nanobubble surface (c_{surf}) as $c_{surf} = H_k P_{NB}$, where P_{NB} is the internal nanobubble pressure and H_k is the Henry's law constant. We neglect small hydrostatic forces to assume the bulk electrolyte pressure (P_{el}) equal to atmospheric pressure (Fig. 4C). We then use a pressure balance at the spherical nanobubble cap to define $P_{NB} = P_{el} + \Delta P_L$, where ΔP_L is the two-phase Laplace pressure difference. For a spherical interface, $\Delta P_L = 2\gamma \sin(\varphi_{NB})/r_{NB}$ (51), where φ_{NB} is the three-phase contact angle, r_{NB} is the nanobubble radius, and γ is the air-water surface tension.

P_{NB} and c_{surf} therefore depend on the nanobubble geometry (fig. S19). Experimentally, the small nanopipette radius constrains r_{NB} to ensure that $c_{surf} > c_{sat} = H_k P_{atm}$, where c_{sat} is the saturated air concentration. This concentration gradient drives gas efflux through the spherical nanobubble caps. The efflux is likely minimized by small φ_{NB} (1), as indicated by the small ΔP_L (green lines) equating P_{el} (black curve) and P_{NB} (blue line) (fig. 4C).

When $\varphi_{NB} < 30°$, the different interfacial geometries result in a Laplace pressure difference across the cylindrical nanobubble region ($\Delta P_L = \gamma/r_{NB}$) that exceeds ΔP_L in the spherical cap region. These conditions bring the interfacial electrolyte under tension, as shown by the larger ΔP_L at the nanobubble's center (Fig. 4C). For a sufficiently thin interfacial electrolyte, the tension is exacerbated by the attractive disjoining pressure (ΔP_Π) between the nanobubble surface and the nanopipette wall (fig. S20) (51–53).

Because of being under tension, the gas solubility of the interfacial electrolyte increases (54) to support nanobubble growth (Fig. 4C, red dashed curve). Multiple additional factors may contribute to gas enrichment in the interfacial electrolyte: Nanobubbles hold highly dense gas (9), nanochannel confinement can bring a bulk fluid under tension (49, 50, 55), and hydrophobic interfaces promote gas enrichment (56) and deplete water density (57).

Finite element modeling and gas law relations enable us to estimate the dissolved gas concentration in the interfacial electrolyte (note S3). For simplicity, we assumed axially oriented nanobubble growth with one spherical cap pinned at the nanopipette opening (49). The ideal gas law relates the nanobubble's dynamic height (Fig. 4A, inset) to its gas accumulation during growth, while a finite element model quantifies efflux through the nanobubble caps. This efflux is primarily determined by φ_{NB}, mostly occurs through the pinned cap (fig. S21), and is considered to remain constant because of the nanobubble height remaining small with respect to the nanopipette length (several centimeters). We quantified gas influx through the interfacial electrolyte as the sum of the spherical cap efflux and the gas accumulation underlying growth. Last, we determined the gas concentration at the nanopipette wall based on a radial concentration gradient across the interfacial electrolyte.

The model predicts that the interfacial electrolyte needs to hold only slightly more dissolved air than is present at the nanobubble surface. In the small φ_{NB} regime, we observe a linear relationship between c_{surf} and φ_{NB} (Fig. 4D, black line), where c_{surf} is plotted after normalization by the saturated gas concentration (c_{sat}). Slow growth and high aspect ratio dimensions ensure that at the nanopipette wall, the dissolved gas concentration needs to be only 0.05 to 0.25% greater than at the nanobubble surface (Fig. 4D, dashed red curves). This excess gas concentration scales with the interfacial electrolyte thickness because more gas is required to maintain an equivalent gradient across a thicker film.

DISCUSSION

Our study characterizes ion transport through nanobubble-plugged nanopipettes and nanobubble metastability under these conditions. We demonstrate composite nanochannels with tunable ionic currents and ion rectification ratios, atomically thin electrolyte films, and effective apertures comparably sized to biological ion channels. We also demonstrate the capability of nanobubbles to enhance nanochannel conductivity in the forward rectification direction, which we attribute to nonlinear electrokinetic phenomena. To attain these results, we developed a mechanical technique for easily fabricating these systems by generating nanobubbles inside nanopipettes.

Crucially, more precise nanobubble formation and dissipation is required to engineer these promising transport properties into ionic sensors, pumps, or filters. Dynamic and controlled nanobubble manipulation may be possible with nanochannel surface functionalization, localized electrochemical activity, or targeted ultrasound stimulation. Better understanding of the transport effects studied here are also relevant to applications relying on ionic currents through nanopipettes, including patch clamp electrophysiology (58, 59) and scanning ion conductance microscopy (59, 60). By observing long-term nanobubble growth without an external source of gas oversaturation, we also present a system that may provide additional insight into three-phase interface dynamics.

MATERIALS AND METHODS

Nanopipette fabrication and modification

Nanopipettes were fabricated from fire-polished quartz capillaries with outer diameters of 1.0 mm, inner diameters of 0.5 mm, and filaments (Sutter Instrument, no. QF100-50-7.5), using a P-2000 laser-based micropipette puller (Sutter Instrument). Nanopipettes were pulled with the single line program: Heat 850 | Fil 5 | Vel 55 | Del 145 | Pul 195. Certain nanopipettes were modified by filling pipette interiors with a 1 weight % solution of poly-L-lysine (Sigma-Aldrich, no. P1399) in deionized (DI) water and subsequently baking them in a 95°C oven until the filling solution evaporated. This treatment coated inner nanopipette walls to be positively charged.

Electrolyte preparation and characterization

Electrolytes were prepared by adding KCl (Thermo Fisher Scientific, no.7447-40-7) to ultraviolet (UV)–treated DI water (18 megohms/cm; Evoqua) and filtering through 0.2-μm pore filters (Thermo Fisher Scientific, no. 566-0020). Electrolyte pH was raised to 7 (or 12, where indicated) via dropwise addition of 1 M KOH (Thermo Fisher Scientific, no. P250). Electrolyte pH was reduced to 2 (where indicated) via dropwise addition of 37% HCl (Thermo Fisher Scientific, no. A144C-212). Electrolyte pH was measured with indicator strips (Millipore, no. 109535). Resistivity of 3 M KCl was determined by measuring the resistance across an electrolyte-filled capillary of known dimensions (Sutter Instrument, no. QF100-50-7.5).

Mechanical nanobubble generation and modification

Nanobubbles were generated upon backfilling nanopipettes with electrolyte and immersing nanopipettes in electrolyte baths. Nanobubble configurations were manipulated by repeated removal and reimmersion of nanopipettes into electrolyte baths. For longevity tests, nanopipettes remained undisturbed inside the electrolyte baths for the durations of the measurement sets.

Electronic characterization

Electronic measurements were performed by applying voltages to Ag/AgCl wire electrodes (A-M Systems, no. 781500) inside nanopipettes and measuring ionic currents through Ag/AgCl disk electrodes (A-M Systems, no. 550025) in electrolyte baths. Electrodes were connected to an Axon MultiClamp 700B amplifier through an Axon CV-7B headstage. Electronic signals were recorded by a data acquisition (DAQ) card (National Instruments, no. PCIe-6353) at 200 kS/s. Through the DAQ, a PC sent voltage waveforms to the amplifier and received current outputs. Current data were analyzed using custom MATLAB programs. For DC conductance measurements, triangle waveforms (−1 to 1 V) were applied at speeds of 1 V/s, 10 V/s, 100 V/s, and 1 V/ms. Waveforms were applied six times, with three starting at −1 V and three starting at 1 V. Reported ionic currents represent the means and SDs measured across these inputs. For AC impedance measurements, 20 mV$_{pk-pk}$ sinusoid waveforms were applied at increasing frequencies. Impedance magnitudes were based on the peak to peak current differences. Phase angles were based on the temporal delay between the peaks of the voltage and current sinusoids. For noise measurements, constant voltages were applied for 5 s, with the first half discarded as settling time. Noise data were smoothed with moving average filters across N points, with $N = \{1, 10, 25, 100\}$ for frequency decades {1-10, 10-100, 100-1000, 1000+}. Noise spikes at harmonics of the 60-Hz grid frequency were removed by hand.

Cryogenic transmission EM

After electrical testing, nanopipette tips were hand-mounted onto transmission EM (TEM) grids (Ted Pella, no. 1GC50) with edges secured by UV-curable epoxy (EPO-TEK, no. OG133-8). The nanopipette-mounted grids were rapidly plunged into liquid nitrogen–cooled liquid ethane (−183°C) with a Vitrobot IV (FEI) using 100% humidity conditions. Cryogenically frozen grids were quickly transferred to a storage box and held in liquid nitrogen until imaging. Micrographs were acquired with the K2 Summit direct electron detector (Gatan) on a Tecnai F20 (FEI) operating at 200 kV. To prevent nanopipette damage from the incident electron beam (as evidenced by melting of the nanopipette tip), very low dose rates (0.1 to 0.5 e$^-$ pixel^{-1} s^{-1}) were used along with quick operation to localize and focus on nanopipette tips. Images were recorded as stacks of 40 frames with a total exposure time of 4 s and a dose rate of 2 e$^-$ pixel^{-1} s^{-1}. Single micrographs were summated from frame stacks using the average algorithm in Digital Micrograph software (Gatan).

Finite element modeling

Ionic currents and nanobubble gas exchange were simulated with the finite element approach (COMSOL Multiphysics 5.4). Automatically generated model reports will be made available upon request. All finite element simulations were considered sufficiently optimized when further mesh refinement no longer altered the ensuing solutions and mass continuities were preserved across domain boundaries. Extensive overviews of the governing physics and model implementations are included in the Supplementary Materials.

Scanning EM

Certain nanopipettes were inspected under scanning EM (SEM) to verify that tips did not break during testing and to fit finite element models to experimental nanopipette geometries. Before inspection, these nanopipettes were baked in a 95°C oven until the filling electrolyte evaporated. Scanning electron micrographs were acquired with the direct electron detector on a Sigma Field Emission SEM (Zeiss) operating at 1 kV. Small working distances (<2 mm) permitted nanoscopic imaging resolution at 1 kV without metal coating of pipette tips.

SUPPLEMENTARY MATERIALS

Supplementary material for this article is available at http://advances.sciencemag.org/cgi/content/full/6/46/eabd0126/DC1

REFERENCES AND NOTES

1. D. Lohse, X. Zhang, Surface nanobubbles and nanodroplets. *Rev. Mod. Phys.* **87**, 981–1035 (2015).
2. P. S. Epstein, M. S. Plesset, On the stability of gas bubbles in liquid-gas solutions. *J. Chem. Phys.* **18**, 1505–1509 (1950).
3. S. Ljunggren, J. C. Eriksson, The lifetime of a colloid-sized gas bubble in water and the cause of the hydrophobic attraction. *Colloid. Surface. A.* **129–130**, 151–155 (1997).
4. M. Blander, J. L. Katz, Bubble nucleation in liquids. *AIChE J.* **21**, 833–848 (1975).
5. X. Zhang, D. Y. C. Chan, D. Wang, N. Maeda, Stability of interfacial nanobubbles. *Langmuir* **29**, 1017–1023 (2013).
6. P. Attard, The stability of nanobubbles. *Eur. Phys. J. Spec. Top.* **223**, 893–914 (2014).
7. J. H. Weijs, D. Lohse, Why surface nanobubbles live for hours. *Phys. Rev. Lett.* **110**, 054501 (2013).
8. M. P. Brenner, D. Lohse, Dynamic equilibrium mechanism for surface nanobubble stabilization. *Phys. Rev. Lett.* **101**, 214505 (2008).
9. L. Zhou, X. Wang, H.-J. Shin, J. Wang, R. Tai, X. Zhang, H. Fang, W. Xiao, L. Wang, C. Wang, X. Gao, J. Hu, L. Zhang, Ultrahigh density of gas molecules confined in surface nanobubbles in ambient water. *J. Am. Chem. Soc.* **142**, 5583–5593 (2020).
10. R. M. M. Smeets, U. F. Keyser, M. Y. Wu, N. H. Dekker, C. Dekker, Nanobubbles in solid-state nanopores. *Phys. Rev. Lett.* **97**, 088101 (2006).
11. M. R. Powell, L. Cleary, M. Davenport, K. J. Shea, Z. S. Siwy, Electric-field-induced wetting and dewetting in single hydrophobic nanopores. *Nat. Nanotechnol.* **6**, 798–802 (2011).
12. S. N. Smirnov, I. V. Vlassiouk, N. V. Lavrik, Voltage-gated hydrophobic nanopores. *ACS Nano* **5**, 7453–7461 (2011).
13. G. Xie, P. Li, Z. Zhao, Z. Zhu, X.-Y. Kong, Z. Zhang, K. Xiao, L. Wen, L. Jiang, Light- and electric-field-controlled wetting behavior in nanochannels for regulating nanoconfined mass transport. *J. Am. Chem. Soc.* **140**, 4552–4559 (2018).
14. G. Xie, K. Xiao, Z. Zhang, X.-Y. Kong, Q. Liu, P. Li, L. Wen, L. Jiang, A bioinspired switchable and tunable carbonate-activated nanofluidic diode based on a single nanochannel. *Angew. Chem. Int. Edit.* **54**, 13664–13668 (2015).
15. Y.-L. Ying, Y.-X. Hu, R. Gao, R.-J. Yu, Z. Gu, L. P. Lee, Y.-T. Long, Asymmetric nanopore electrode-based amplification for electron transfer imaging in live cells. *J. Am. Chem. Soc.* **140**, 5385–5392 (2018).
16. J. Lee, T. Laoui, R. Karnik, Nanofluidic transport governed by the liquid/vapour interface. *Nat. Nanotechnol.* **9**, 317–323 (2014).
17. X. Hou, Y. Hu, A. Grinthal, M. Khan, J. Aizenberg, Liquid-based gating mechanism with tunable multiphase selectivity and antifouling behaviour. *Nature* **519**, 70–73 (2015).
18. P. Aryal, M. S. P. Sansom, S. J. Tucker, Hydrophobic gating in ion channels. *J. Mol. Biol.* **427**, 121–130 (2015).
19. G. Pérez-Mitta, A. S. Peinetti, M. L. Cortez, M. E. Toimil-Molares, C. Trautmann, O. Azzaroni, Highly sensitive biosensing with solid-state nanopores displaying enzymatically reconfigurable rectification properties. *Nano Lett.* **18**, 3303–3310 (2018).
20. M. Lepoitevin, G. Nguyen, M. Bechelany, E. Balanzat, J.-M. Janot, S. Balme, Combining a sensor and a pH-gated nanopore based on an avidin-biotin system. *Chem. Commun.* **51**, 5994–5997 (2015).
21. J. R. Burns, A. Seifert, N. Fertig, S. Howorka, A biomimetic DNA-based channel for the ligand-controlled transport of charged molecular cargo across a biological membrane. *Nat. Nanotechnol.* **11**, 152–156 (2016).
22. Q. Liu, K. Xiao, L. Wen, H. Lu, Y. Liu, X.-Y. Kong, G. Xie, Z. Zhang, Z. Bo, L. Jiang, Engineered ionic gates for ion conduction based on sodium and potassium activated nanochannels. *J. Am. Chem. Soc.* **137**, 11976–11983 (2015).
23. X. Hou, W. Guo, L. Jiang, Biomimetic smart nanopores and nanochannels. *Chem. Soc. Rev.* **40**, 2385–2401 (2011).
24. I. Vlassiouk, T. R. Kozel, Z. S. Siwy, Biosensing with nanofluidic diodes. *J. Am. Chem. Soc.* **131**, 8211–8220 (2009).
25. A. Agarwal, W. J. Ng, Y. Liu, Principle and applications of microbubble and nanobubble technology for water treatment. *Chemosphere* **84**, 1175–1180 (2011).
26. M. Fan, D. Tao, R. Honaker, Z. Luo, Nanobubble generation and its applications in froth flotation (part II): Fundamental study and theoretical analysis. *Min. Sci. Technol.* **20**, 159–177 (2010).

27. A. P. Straub, N. Y. Yip, S. Lin, J. Lee, M. Elimelech, Harvesting low-grade heat energy using thermo-osmotic vapour transport through nanoporous membranes. *Nat. Energy* **1**, 16090 (2016).

28. M. A. Edwards, H. S. White, H. Ren, Voltammetric determination of the stochastic formation rate and geometry of individual H_2,N_2, and O_2 bubble nuclei. *ACS Nano* **13**, 6330–6340 (2019).

29. Y. Wang, X. Li, Y. Zhou, P. Huang, Y. Xu, Preparation of nanobubbles for ultrasound imaging and intracelluar drug delivery. *Int. J. Pharm.* **384**, 148–153 (2010).

30. H. J. Schenk, K. Steppe, S. Jansen, Nanobubbles: A new paradigm for air-seeding in xylem. *Trends Plant Sci.* **20**, 199–205 (2015).

31. H. S. White, A. Bund, Ion current rectification at nanopores in glass membranes. *Langmuir* **24**, 2212–2218 (2008).

32. R. B. Schoch, J. Han, P. Renaud, Transport phenomena in nanofluidics. *Rev. Mod. Phys.* **80**, 839–883 (2008).

33. T. M. Squires, M. Z. Bazant, Induced-charge electro-osmosis. *J. Fluid Mech.* **509**, 217–252 (2004).

34. S. J. Kim, Y. C. Wang, J. H. Lee, H. Jang, J. Han, Concentration polarization and nonlinear electrokinetic flow near a nanofluidic channel. *Phys. Rev. Lett.* **99**, 044501 (2007).

35. J. Rabinowitz, M. A. Edwards, E. Whittier, K. Jayant, K. L. Shepard, Nanoscale fluid vortices and nonlinear electroosmotic flow drive ion current rectification in the presence of concentration gradients. *J. Phys. Chem. A* **123**, 8285–8293 (2019).

36. R. M. M. Smeets, U. F. Keyser, N. H. Dekker, C. Dekker, Noise in solid-state nanopores. *Proc. Natl. Acad. Sci. U.S.A.* **105**, 417–421 (2008).

37. K. A. Karraker, C. J. Radke, Disjoining pressures, zeta potentials and surface tensions of aqueous non-ionic surfactant/electrolyte solutions: Theory and comparison to experiment. *Adv. Colloid Interface Sci.* **96**, 231–264 (2002).

38. A. Plecis, R. B. Schoch, P. Renaud, Ionic transport phenomena in nanofluidics: Experimental and theoretical study of the exclusion-enrichment effect on a chip. *Nano Lett.* **5**, 1147–1155 (2005).

39. Q. Pu, J. Yun, H. Temkin, S. Liu, Ion-enrichment and ion-depletion effect of nanochannel structures. *Nano Lett.* **4**, 1099–1103 (2004).

40. D. Shin, J. B. Park, Y.-J. Kim, S. J. Kim, J. H. Kang, B. Lee, S.-P. Cho, B. H. Hong, K. S. Novoselov, Growth dynamics and gas transport mechanism of nanobubbles in graphene liquid cells. *Nat. Commun.* **6**, 6068 (2015).

41. R. Chen, R. J. Balla, A. Lima, S. Amemiya, Characterization of nanopipet-supported ITIES tips for scanning electrochemical microscopy of single solid-state nanopores. *Anal. Chem.* **89**, 9946–9952 (2017).

42. A. Al-Amoudi, J.-J. Chang, A. Leforestier, A. McDowall, L. M. Salamin, L. P. O. Norlén, K. Richter, N. S. Blanc, D. Studer, J. Dubochet, Cryo-electron microscopy of vitreous sections. *EMBO J.* **23**, 3583–3588 (2004).

43. D. P. Hoogerheide, S. Garaj, J. A. Golovchenko, Probing surface charge fluctuations with solid-state nanopores. *Phys. Rev. Lett.* **102**, 256804 (2009).

44. S. Buyukdagli, M. Manghi, J. Palmeri, Ionic exclusion phase transition in neutral and weakly charged cylindrical nanopores. *J. Chem. Phys.* **134**, 074706 (2011).

45. E. Karatay, A. S. Haase, C. W. Visser, C. Sun, D. Lohse, P. A. Tsai, R. G. H. Lammertink, Control of slippage with tunable bubble mattresses. *Proc. Natl. Acad. Sci. U.S.A.* **110**, 8422–8426 (2013).

46. S. Umehara, N. Pourmand, C. D. Webb, R. W. Davis, K. Yasuda, M. Karhanek, Current rectification with poly-L-lysine-coated quartz nanopipettes. *Nano Lett.* **6**, 2486–2492 (2006).

47. J. Lyklema, M. Minor, On surface conduction and its role in electrokinetics. *Colloid. Surface. A.* **140**, 33–41 (1998).

48. D. Stein, M. Kruithof, C. Dekker, Surface-charge-governed ion transport in nanofluidic channels. *Phys. Rev. Lett.* **93**, 035901 (2004).

49. C. Duan, R. Karnik, M.-C. Lu, A. Majumdar, Evaporation-induced cavitation in nanofluidic channels. *Proc. Natl. Acad. Sci. U.S.A.* **109**, 3688–3693 (2012).

50. O. Vincent, A. Szenicer, A. D. Stroock, Capillarity-driven flows at the continuum limit. *Soft Matter* **12**, 6656–6661 (2016).

51. B. V. Derjaguin, N. V. Churaev, V. M. Muller, *Surface Forces* (Springer, 1987).

52. W. Dhaouadi, J. M. Kolinski, Bretherton's buoyant bubble. *Phys. Rev. Fluids.* **4**, 123601 (2019).

53. F. L. Leite, C. C. Bueno, A. L. Da Róz, E. C. Ziemath, O. N. Oliveira Jr., Theoretical models for surface forces and adhesion and their measurement using atomic force microscopy. *Int. J. Mol. Sci.* **13**, 12773–12856 (2012).

54. P. Lidon, S. C. Marker, J. J. Wilson, R. M. Williams, W. R. Zipfel, A. D. Stroock, Enhanced oxygen solubility in metastable water under tension. *Langmuir* **34**, 12017–12024 (2018).

55. N. R. Tas, P. Mela, T. Kramer, J. W. Berenschot, A. Van Den Berg, Capillarity induced negative pressure of water plugs in nanochannels. *Nano Lett.* **3**, 1537–1540 (2003).

56. C. Sendner, D. Horinek, L. Bocquet, R. R. Netz, Interfacial water at hydrophobic and hydrophilic surfaces: Slip, viscosity, and diffusion. *Langmuir* **25**, 10768–10781 (2009).

57. D. A. Doshi, E. B. Watkins, J. N. Israelachvili, J. Majewski, Reduced water density at hydrophobic surfaces: Effect of dissolved gases. *Proc. Natl. Acad. Sci. U.S.A.* **102**, 9458–9462 (2005).

58. K. Jayant, M. Wenzel, Y. Bando, J. P. Hamm, N. Mandriota, J. H. Rabinowitz, I. Jen-La Plante, J. S. Owen, O. Sahin, K. L. Shepard, R. Yuste, Flexible nanopipettes for minimally invasive intracellular electrophysiology in vivo. *Cell Rep.* **26**, 266–278.e5 (2019).

59. P. Novak, J. Gorelik, U. Vivekananda, A. I. Shevchuk, Y. S. Ermolyuk, R. J. Bailey, A. J. Bushby, G. W. J. Moss, D. A. Rusakov, D. Klenerman, D. M. Kullmann, K. E. Volynski, Y. E. Korchev, Nanoscale-targeted patch-clamp recordings of functional presynaptic ion channels. *Neuron* **79**, 1067–1077 (2013).

60. P. Novak, C. Li, A. I. Shevchuk, R. Stepanyan, M. Caldwell, S. Hughes, T. G. Smart, J. Gorelik, V. P. Ostanin, M. J. Lab, G. W. J. Moss, G. I. Frolenkov, D. Klenerman, Y. E. Korchev, Nanoscale live-cell imaging using hopping probe ion conductance microscopy. *Nat. Methods* **6**, 279–281 (2009).

Citation: J. Rabinowitz, E. Whittier, Z. Liu, K. Jayant, J. Frank, K. Shepard, Nanobubble-controlled nanofluidic transport. *Sci. Adv.* **6**, eabd0126 (2020).

Science Advances

Nanobubble-controlled nanofluidic transport

Jake Rabinowitz, Elizabeth Whittier, Zheng Liu, Krishna Jayant, Joachim Frank and Kenneth Shepard